

Optimizing electromagnetic sensors for unexploded ordnance detection

Stephen Billings¹ and Laurens Beran¹

ABSTRACT

Time-domain electromagnetic (TEM) instruments are the predominant geophysical sensor for detection of buried unexploded ordnance (UXO). Detection surveys commonly use towed TEM sensor arrays to acquire a digital map for target detection. We use a dipolar model to predict a detection threshold for a UXO at a specified clearance depth, given an arbitrary sensor geometry. In general, the minimum target response is obtained for a horizontally oriented target. We find that for multistatic sensors, the minimum response can also depend on the azimuth of the target. By considering the statistics of the target response, we find that the detection threshold can be raised slightly while still ensuring a high probability of detection of UXO at depth. This increase in the detection threshold can have a significant effect on the number of false alarms that need to be interrogated or investigated and hence on the cost of clearance. We also use Monte Carlo simulation to investigate how array geometry and height affect clutter rejection.

INTRODUCTION

Time-domain electromagnetic (TEM) instruments are the most commonly used geophysical sensor for detection and classification of buried unexploded ordnance (UXO). Although magnetic sensors can detect ordnance with ferrous components, a magnetic soil response can often produce false alarms and obscure the signal from a UXO (Butler, 2003). Similarly, ground-penetrating radar (GPR) is primarily sensitive to contrasts in dielectric permittivity and can produce numerous false alarms in the presence of soil inhomogeneities (Billings and Kingdon, 2008; Everett, 2013).

TEM data can be processed to minimize the effects of ferromagnetic soils, for example by removing an estimated half-space soil response from the observed data (Pasion et al., 2007). There is also a strong electrical conductivity contrast between buried ordnance

and background response that significantly reduces false alarm rates relative to GPR. Finally, TEM data can be inverted to recover parameters related to intrinsic target properties (size, shape, and material composition). These parameters are subsequently used to discriminate between ordnance and harmless metallic clutter (Bell et al., 2001; Pasion and Oldenburg, 2001).

For these reasons, TEM systems have been the focus of research in UXO detection and classification, leading to a proliferation of sensor geometries. In this paper, we focus on the Geonics EM-61, which is often deployed as a vehicle-towed array by combining multiple coils for an initial detection survey. Subsequent cued interrogations revisit targets identified in the detection data with a multistatic, multicomponent sensor. The cued data are then processed to generate a prioritized dig list that seeks to identify all ordnance with a minimal number of false alarms. Recent demonstrations of this procedure have achieved false alarms rates of 2:1 (two non-UXO for every UXO found) or lower (Beran et al., 2012; Shamatava et al., 2012). This is a significant improvement over the 100:1 false alarm rates typically achieved without classification (Delaney and Eter, 2003).

In this paper, we consider how arrays of EM-61 coils can be optimized to detect buried UXO. We do not consider the issue of classification, which is well-covered elsewhere (e.g., Beran et al., 2012; Shamatava et al., 2012; Bijamov et al., 2014). We first discuss how a detection threshold can be modeled for a given ordnance type at a specified maximum depth. In practice, we find that this threshold can generate a very high number of target picks. We therefore consider how the statistics of target response can be modeled to obtain a slightly higher threshold that maintains a high probability of detecting all UXO at depth. Sensor geometry and height play an important role in target detection, and we investigate how these factors can be varied to minimize detection of near-surface metallic clutter.

MODELING DETECTION THRESHOLDS

Targets identified in a detection mode survey must be selected for subsequent excavation or cued interrogation using objective and reproducible criteria. The geophysical system verification (GSV)

Manuscript received by the Editor 2 May 2016; revised manuscript received 23 September 2016; published online 20 February 2017.

¹Black Tusk Geophysics, Vancouver, British Columbia, Canada. E-mail: stephenbillings@btgeophysics.com; laurens.beran@btgeophysics.com.

© 2017 Society of Exploration Geophysicists. All rights reserved.

approach developed by Nelson et al. (2010) advocates setting a target-picking threshold based on the lowest predicted amplitude expected for targets of interest at a specified clearance depth.

GSV detection analysis uses a time-varying magnetic dipole to model the response of a buried UXO. The secondary magnetic field \mathbf{B}_s radiated by a buried target is given by

$$\mathbf{B}_s(\mathbf{r}, t) = \frac{\mu_0}{r^3} (3(\hat{\mathbf{p}}(t) \cdot \hat{\mathbf{r}})\hat{\mathbf{r}} - \hat{\mathbf{p}}(t)), \quad (1)$$

where \mathbf{r} is the separation between the target and observation location and $\mathbf{p}(t)$ is the time-varying dipole moment. The induced dipole moment is computed as the projection of the primary magnetic field \mathbf{B}_0 onto the target's polarizability tensor $\mathbf{P}(t)$ (Bell et al., 2001; Pasion and Oldenburg, 2001)

$$\mathbf{p}(t) = \frac{1}{\mu_0} \mathbf{P}(t) \cdot \mathbf{B}_0. \quad (2)$$

The polarizability tensor is assumed to be symmetric and positive definite, and so it can be decomposed as

$$\mathbf{P}(t) = \mathbf{A}\mathbf{L}(t)\mathbf{A}^T, \quad (3)$$

where \mathbf{A} is the orthogonal matrix, which rotates the coordinate system from geographic coordinates to a local, body-centered coordinate system. The rotation matrix \mathbf{A} can be parameterized by the target's dip, azimuth, and roll (ϕ, θ, γ). The diagonal eigenvalue matrix $\mathbf{L}(t)$ contains the principal polarizabilities $L_i(t)$ ($i = 1, 2, 3$), which are assumed to be independent of the target orientation and location

and can therefore be used for target classification. Ferrous UXOs are characterized by a dominant, slow-decaying primary polarizability that is aligned with the axis of symmetry. The smaller, transverse (L_2, L_3) polarizabilities are orthogonal to the axial polarizability. The equality of transverse polarizabilities ($L_2 = L_3$) is diagnostic of ordnance with a circular cross section.

To model the lowest amplitude response of a UXO illuminated by a monostatic sensor, GSV analysis in Nelson et al. (2010) considers a horizontal target with the azimuth oriented perpendicular to the sensor track. In this orientation, the primary field is decoupled from the axial (L_1) polarizability of the target, so that the dipole response is dominated by the sum of the smaller, transverse polarizabilities.

However, for arrays of EM-61 sensors with transmitters firing simultaneously, we find that the target orientation producing a minimum response is also horizontal, but it may not necessarily be perpendicular to the sensor track as it is with a single EM-61 sensor. This is illustrated in Figures 1 and 2, which compare the predicted response of a 37 mm projectile at 30 cm depth, illuminated by two different arrays of EM-61 sensors. In both cases, the sensor is 20 cm above the ground.

To generate the target polarizabilities for the EM61 sensor, test-pit measurements were acquired directly over the ordnance item in the horizontal and vertical orientations. The vertical measurement provides an estimate of the axial polarizability $L_1(t_j)$, whereas the horizontal measurements provide an estimate of the transverse polarizabilities ($L_2(t_j)$ and $L_3(t_j)$) at the four time gates t_j of the EM61 (centered at 0.216, 0.366, 0.66, and 1.266 ms).

In Figure 1a and 1b, we show the amplitude of the predicted response at a grid of target locations, for along-track and cross-track azimuthal orientations of the target, respectively.

In Figure 1a, the maximum response in the along-track orientation occurs at the leading and trailing edges of the array where the field underneath the array has a strong along-track component that couples with the primary polarizability of the object. Conversely, in the cross-track orientation (Figure 1b), the primary field aligns with the primary polarizability at the sides of the array, thereby producing response maxima at the left and right edges of the array.

For each target orientation, we select the maximum value at each cross-track position to estimate the minimum anomaly amplitude obtained when the sensor passes over the target (Figure 1c). Thus, although an along-track orientation produces a weak response when the array is directly over the target, it produces a much stronger response at the leading and trailing edges of the array. The along-track orientation only becomes the worst orientation near the edges of the array, where the cross-track orientation produces a very strong response. In the central section of the array, and for this particular geometry, the cross-track orientation produces the limiting response. The global minimum of the response (≈ 7.4 mV at channel 3) is near the cross-track edges of the center transmitter coil.

Note that in this analysis, we also consider the intermediate azimuthal orientations to determine

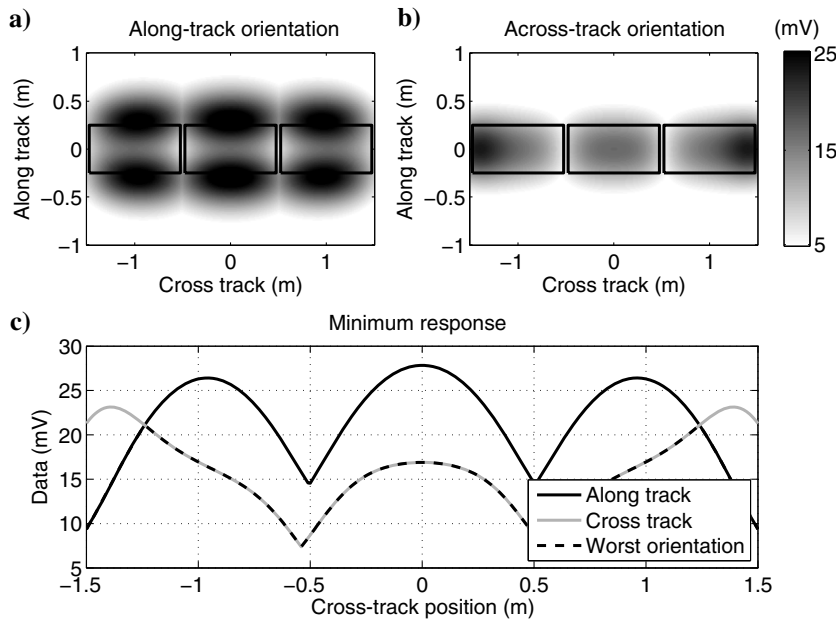


Figure 1. Anomaly amplitude analysis for a horizontal 37 mm projectile at 30 cm depth illuminated by a three-coil EM-61 array. (a) Anomaly amplitude (mV) at channel 3 as a function of target location, for a target oriented along track. The white areas of the plot correspond to amplitudes less than 6 mV, whereas the black lines indicate transmitters. (b) As in panel (a), but with horizontal target oriented across track. (c) Minimum of responses in panels (a and b) across the swath of the sensor array. "Worst orientation" also considers intermediate target azimuths, in this case, the minimum response always corresponds to the limiting cross-track and along-track orientations.

the minimum response of a horizontal target at any cross-track location. We can save some computational effort at this step by analytically minimizing the measured vertical response in a loop receiver with respect to the target azimuth, as described in Appendix A.

For the three-coil array in Figure 1, the minimum response always corresponds to the limiting cross-track and along-track target orientations. In Figure 2, we repeat the threshold analysis for a pyramid configuration of three sensors, with one sensor placed between and forward of the other two sensors. Here, the worst azimuthal orientation is not necessarily in the cross-track or along-track positions; the minimum azimuth in this case can be identified using equation A-12.

MODELING A DISTRIBUTION OF DETECTION THRESHOLDS

The GSV analysis models a detection threshold based on the worst-case scenario for a buried UXO; i.e., the target is at the maximum specified clearance depth and is in the orientation producing a minimal response amplitude. In practice, target picking down to this threshold can often produce a very large number of picks that must be excavated or interrogated with a cued sensor. For example, at the Jeep and Demolition Range (JDR) at the Former Lowry Bombing and Gunnery Range, CO, we found that a 30 cm clearance depth for 37 mm projectiles, corresponding to a 7.4 mV threshold with a linear three-coil array (Figure 1), required us to dig a prohibitively large number of picks. For example, in one 50×50 m grid, approximately 450 targets were picked, far exceeding the 50 targets/grid expected at this site.

We find that by considering the statistics of the target response, we can raise the detection threshold and significantly reduce the number of target picks, while maintaining a high probability of detecting UXO at the maximum clearance depth. Assuming a uniform spatial distribution of 37 mm projectiles throughout the sensor footprint together with a uniform distribution of target azimuths, we use Monte Carlo simulation to obtain the cumulative distribution of response amplitudes in Figure 3. At 0.99 and 0.95 confidence levels, we can raise the detection threshold in Figure 1 to approximately 9.3 and 12.1 mV, respectively. In Figure 3c, we plot the proportion of 37 mm targets that fall below these thresholds as a function of the cross-track location below the linear three-coil array. For the 9.3 mV threshold (0.99 confidence level), the nonzero regions of targets below the threshold are restricted to lobes near the sides of the transmitter coils. Increasing the threshold to 12.1 mV (0.95 confidence level) increases the chances that a 37 mm target within

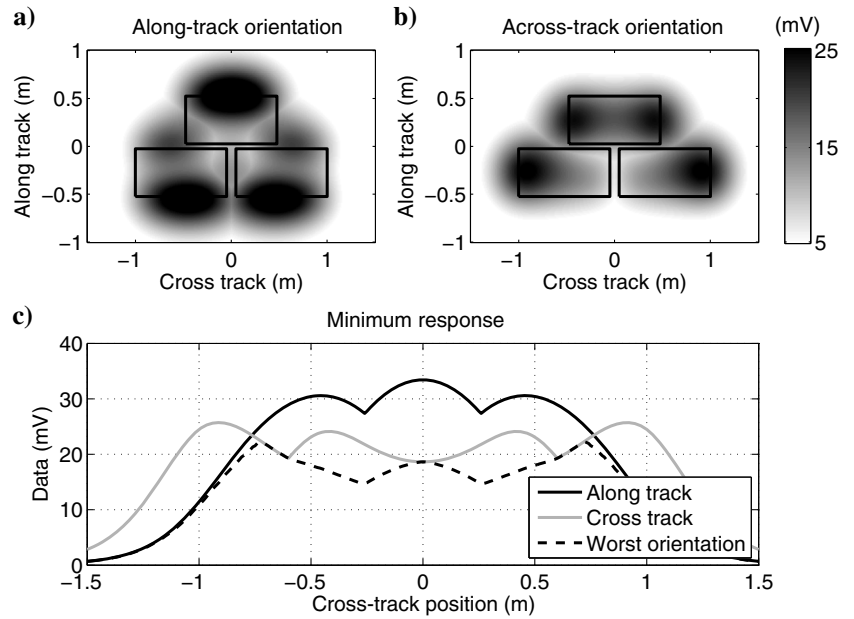


Figure 2. Anomaly amplitude analysis for a pyramid three-coil EM-61 array. Note in this case that the worst-case amplitude does not always correspond to the cross-track orientation.

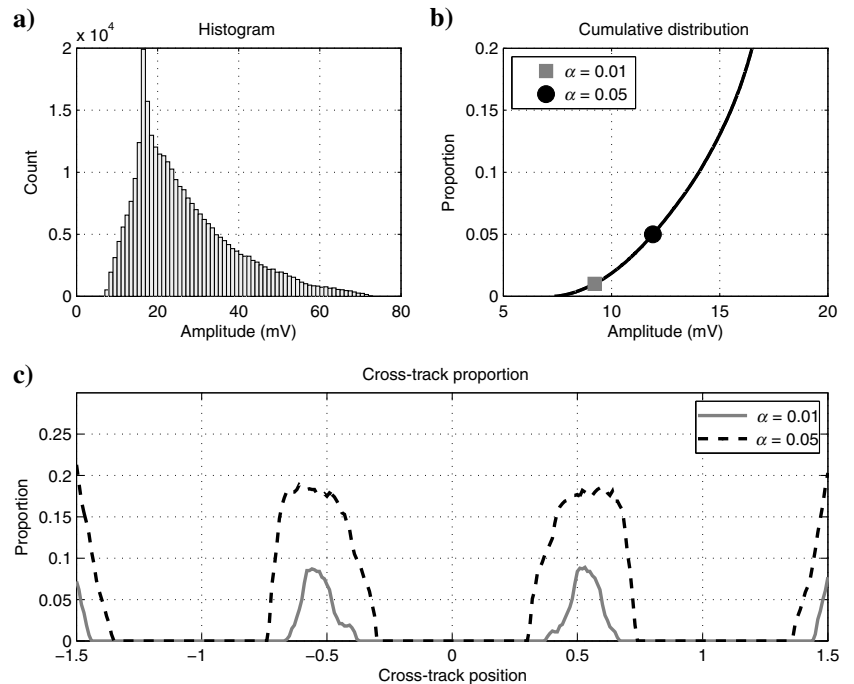


Figure 3. (a) Distribution of response amplitudes for horizontal 37 mm projectiles at 30 cm depth below a three-coil linear array (see Figure 1). Targets are distributed uniformly with respect to the cross-track location and have a uniform random azimuth. (b) Lower tail of the cumulative distribution. Markers indicate the 0.99 and 0.95 confidence bounds. (c) Proportion of horizontal 37 mm targets with a response amplitude below threshold specified by confidence level $1 - \alpha$, as a function of the cross-track location.

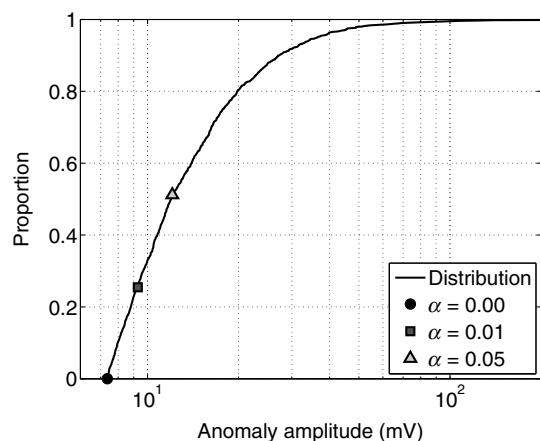


Figure 4. Observed cumulative distribution of response amplitudes for detected targets at JDR. Markers indicate $1 - \alpha$ confidence thresholds for detection of 37 mm targets.

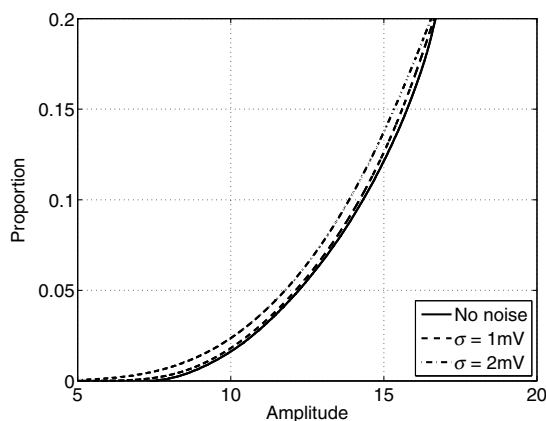
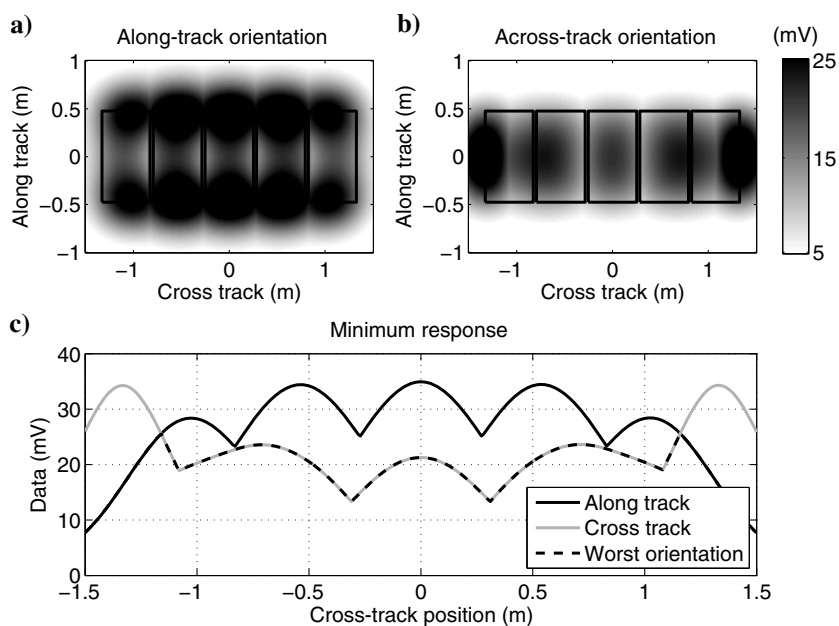


Figure 5. Impact of sensor noise on the cumulative distribution function for a 37 mm projectile at 30 cm.

Figure 6. Anomaly amplitude analysis for a five-coil EM-61 array.



the sensor swath will have an amplitude below the detection threshold.

As shown in Figure 4, increasing the threshold to 9.3 mV at JDR reduced the number of target picks by 25%, while still ensuring a very high confidence of finding all 37 mm projectiles. At the 95% confidence threshold, we have a 51% reduction in target picks.

At sites where the worst-case threshold produces a prohibitive number of picks, this type of statistical analysis can provide objective justification for slightly raising the detection threshold. In particular, stakeholders may be prepared to increase the detection threshold when they realize, for example, that 25% of the digging effort may be expended in covering a 1% probability of a missed 37 mm projectile at the required clearance depth.

After conducting the GSV analysis, it is common to reduce the anomaly threshold to account for noise. Typically, the threshold is reduced by 2σ , where σ is the estimated noise floor. Figure 5 compares cumulative distributions of 37 mm response amplitudes for no noise, $\sigma = 1$ and 2 mV. These distributions are generated with Monte Carlo simulations as shown in Figure 3; here, zero-mean Gaussian noise with standard deviation σ is added to each realization of predicted data. In this case, the effect of noise on the probability of detection is minimal. Even with a comparatively high noise level of 2 mV, the worst-case detection threshold (7.4 mV) translates to only a 0.5% probability of missing a 37 mm at the maximum 30 cm clearance depth.

OPTIMIZING ARRAY DESIGN FOR TARGET DETECTION

We now further explore how array geometry affects the detection threshold. Optimal sensor design was approached in [Smith and Morrison \(2005\)](#) by minimizing expected polarizability variance, as predicted by a linear uncertainty analysis. [Fernandez et al. \(2012\)](#) investigate how different combinations of transmitter coils in a multistatic array can be fired simultaneously to minimize the decay of the primary field and thereby enhance detection of relatively deep (>0.5 m) UXO. Here, we instead consider how the response

amplitudes of UXO and near-surface clutter depend upon sensor geometry. Our goal is to maximize detection of the UXO while minimizing detection of small clutter.

For detection of horizontal targets, the linear three-coil array shown in Figure 1 has obvious weak points just outside the central sensor. This shortcoming is addressed somewhat by the three-coil pyramid configuration in Figure 2. Although the swath width is decreased by this design, the minimum response across the swath is significantly elevated for the asymmetric array from 7.4 to 13 mV (assuming a 1.9 m swath compared with 3 m swath for the original design). Narrowing the swath will decrease the production rate, but this will raise the detection threshold.

However, changing the transmitter/receiver geometry may increase the response amplitude of the clutter and UXO, such that an increase in the minimum amplitude for UXO does not necessarily imply an overall improvement in detection performance. For instance, Figure 6 illustrates the increased amplitudes that occur with a five-element EM-61 array, which has a transmitter moment that is 5/3 times as large as the three-element EM61 arrays. The increased moment also tends to increase the amplitude of the shallower clutter items so that more clutter items will exceed a fixed amplitude threshold. These items typically constitute a significant fraction of non-hazardous items that need to be interrogated or excavated at a site.

To determine if one design is better able than another to reject shallow, near-surface clutter, we compare the fraction of smaller surface items that need to be excavated for the different designs (Figure 7). We assume that the smaller clutter items have the same ratio of primary to secondary polarizabilities as the 37 mm projectile and scale those polarizabilities by “clutter size”: Thus, when the clutter size is 0.1, the clutter has polarizabilities that are 10 times smaller than those for a 37 mm projectile. We use Monte Carlo simulation to obtain a distribution of response amplitudes for a given clutter size, assuming that the clutter is at 0 cm depth and has a uniform distribution of cross-track location and orientation.

The improvement of the three-coil pyramid design over the linear three-coil design is reflected by the decrease in the proportion of clutter of any given size that lies over the detection threshold. Moving to a five-coil pyramid design (two coils forward and between three linear coils) results in a further improvement in clutter rejection and, perhaps more importantly, in an increased swath width. The best of the designs considered is the five-coil linear array shown in Figure 6: The improved performance is partly due to the slower falloff of the primary field with depth for the larger transmitter area and partly due to the tighter lateral spacing of the receiver coils.

The same methodology can be used to determine the best sensor height for a given detection scenario. A low sensor height might be required to achieve good detection of small items, such as a 20 mm projectile. However, a low sensor height can be detrimental when, for example, the minimum-sized item is a 37 mm projectile at 30 cm depth (Figure 8). At a low sensor height of 10 cm, a significant fraction of small near-surface clutter will generate amplitudes above

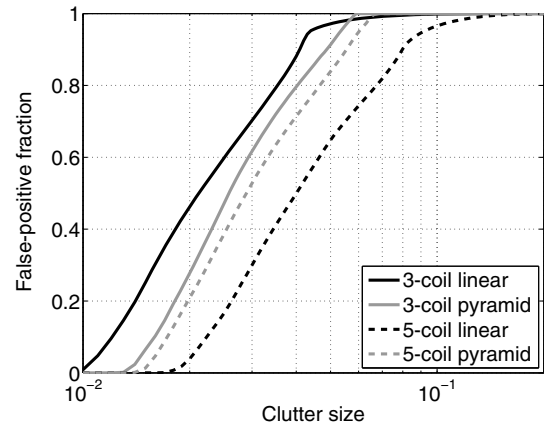


Figure 7. Comparison of the near-surface clutter rejection performance of four different EM-61 array geometries, assuming the smallest UXO is a 37 mm at 30 cm depth. False-positive fraction (FPF) denotes the proportion of clutter of a given size that exceeds the detection threshold for an array. The five-coil linear array consistently achieves the best clutter rejection with the lowest FPF for any given clutter size.

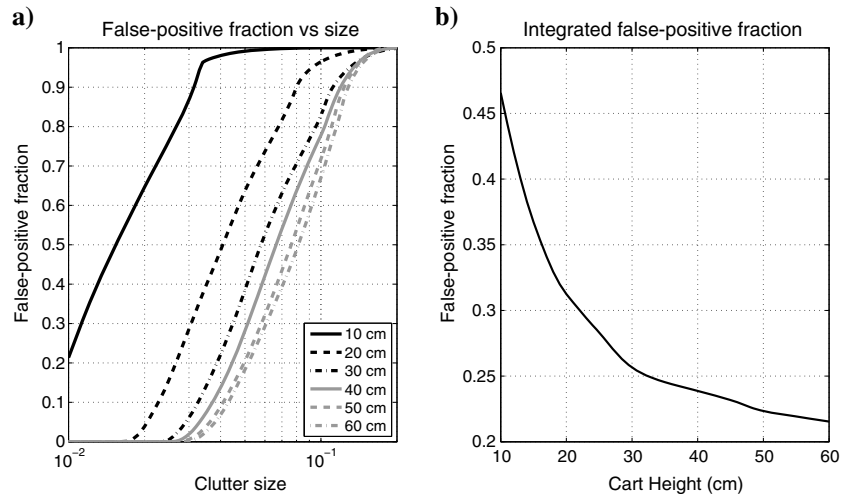


Figure 8. Comparison of the near-surface clutter rejection performance of the five-coil linear EM61 array as a function of sensor height: (a) the false-positive fraction versus size for six array heights and (b) the total false-positive fraction assuming a log-uniform distribution of clutter size.

the detection threshold. As the sensor height is increased, the proportion of clutter excavated decreases. Assuming a log-uniform distribution of clutter between the axis limits of Figure 8a results in the total false-positive fraction (FPF) versus sensor height plot of Figure 8b. The decrease in the FPF fraction with the increased sensor height begins to level off at approximately 30–35 cm, indicating that for this target, a five-coil array height between 35 and 45 cm is ideal. Any further increase in sensor height will result in a decrease in signal to noise at the clearance depth without a significant reduction in false alarms.

CONCLUSION

We have considered how the optimal detection of buried UXO with TEM sensors depends on geometry and height. Arbitrary ar-

rays of monostatic sensors (e.g., EM-61s) can be assembled for a detection survey. Dipole modeling can be used to determine a detection threshold for a UXO at a specified clearance depth. By considering the statistics of the target response, we have shown that the detection threshold for an array can be raised slightly while still ensuring a high probability of detection of UXO at depth. We have also developed techniques for investigating how array geometry and height affect clutter rejection. Of the EM-61 sensor arrays considered, we found that a linear five-coil array detected a minimal proportion of near-surface clutter. Similarly, we show how sensor height can be selected to reduce the signal due to clutter in the detection data while still ensuring detection of UXO.

The methods developed here can be readily extended to newer, multicomponent TEM sensors that have been specifically developed for UXO detection and classification. The same forward modeling can be used to predict detection thresholds, and Monte Carlo simulations can be used to generate a distribution of thresholds for an arbitrary sensor. Future work will focus on exploiting the longer off times of advanced TEM systems to improve rejection of fast-decaying clutter.

ACKNOWLEDGMENTS

This work was funded by the Strategic Environmental Research and Development Program (SERDP) under project MR-2226 “Decision support tools for munitions response performance prediction and risk assessment.”

APPENDIX A

MINIMUM RESPONSE IN A HORIZONTAL RECEIVER FOR A DIPOLE SOURCE

In this section, we develop an efficient approach for identifying the minimum response measured in loop receivers for a given target location. We first derive an expression for the target azimuths producing the minimum and maximum vertical response in a receiver. These extrema are then used to find a simple parametric representation of the dependence of the response over all angles. The electromotive force Φ induced in a horizontal receiver is given by Faraday’s law

$$\Phi = \int_S \mathbf{B} \cdot d\mathbf{s}. \quad (\text{A-1})$$

By Stokes’ law, we evaluate this as the line integral on the boundary

$$\Phi = \int_{\partial S} \mathbf{r} \cdot d\boldsymbol{\ell}, \quad (\text{A-2})$$

with

$$\mathbf{r} = \frac{\mu_o}{4\pi} \frac{\mathbf{p} \times \mathbf{r}}{r^3}, \quad (\text{A-3})$$

the vector potential for a magnetic dipole with dipole moment \mathbf{p} . The position vector between dipole and a point on the receiver loop is \mathbf{r} . Evaluating the line integral (equation A-2) between points \mathbf{r}_i and \mathbf{r}_j on the receiver, we obtain

$$\Phi_{ij} = \alpha_{ij} [\mathbf{p} \cdot (\mathbf{r}_i \times \mathbf{r}_j)], \quad (\text{A-4})$$

with

$$\alpha_{ij} = \frac{\mu_o}{4\pi} \frac{1/|\mathbf{r}_i| + 1/|\mathbf{r}_j|}{|\mathbf{r}_i||\mathbf{r}_j| + \mathbf{r}_i \cdot \mathbf{r}_j}. \quad (\text{A-5})$$

The total electromotive force (emf) in the receiver is then the summation of the emfs over all linear segments comprising the loop

$$\Phi = \mathbf{p} \cdot \tilde{\mathbf{r}}, \quad (\text{A-6})$$

where

$$\tilde{\mathbf{r}} = \sum_{ij} \alpha_{ij} (\mathbf{r}_i \times \mathbf{r}_j). \quad (\text{A-7})$$

The dipole moment is

$$\mathbf{p} = \mathbf{M}\mathbf{B}, \quad (\text{A-8})$$

where \mathbf{B} is the primary field at the dipole location. For a horizontal target, the polarization tensor can be decomposed as

$$\mathbf{M} = \mathbf{A}\mathbf{L}\mathbf{A}^T, \quad (\text{A-9})$$

with polarizabilities $\mathbf{L} = \text{diag}(L_1, L_2, L_3)$. The Euler rotation matrix for a horizontal target with azimuth θ is

$$\mathbf{A} = \begin{pmatrix} \cos(\theta) & \sin(\theta) & 0 \\ -\sin(\theta) & \cos(\theta) & 0 \\ 0 & 0 & 1 \end{pmatrix}. \quad (\text{A-10})$$

Differentiating with respect to θ , we obtain

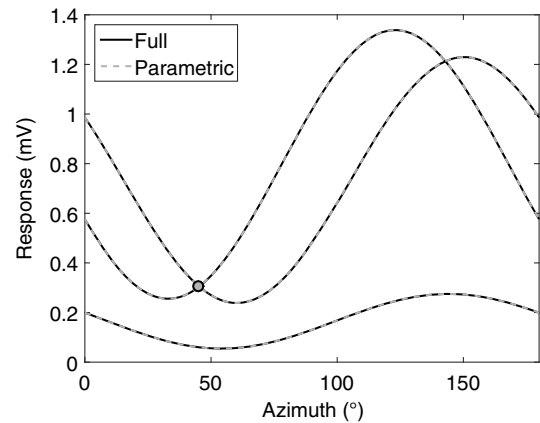


Figure A-1. Dependence of receiver responses on the target azimuth for the three-coil pyramidal array geometry in Figure 2. The solid and dashed lines show results obtained with full forward modeling and a simplified parameterization (equation A-14), respectively. Predicted responses are for a 37 mm projectile at $(x, y) = (-1, 0.55)$ m, relative to the array center. At this location, the maximum response over all receivers is minimized at a target azimuth of 45° , as indicated by the marker.

$$\begin{aligned}\frac{\partial \Phi}{\partial \theta} &= \frac{\partial m_x}{\partial \theta} \tilde{r}_x + \frac{\partial m_y}{\partial \theta} \tilde{r}_y, \\ &= (L_1 - L_2)[(B_y \tilde{r}_y - B_x \tilde{r}_x) \sin(2\theta) \\ &\quad + (B_x \tilde{r}_y + B_y \tilde{r}_x) \cos(2\theta)].\end{aligned}\quad (\text{A-11})$$

Setting $\partial \Phi / \partial \theta = 0$, we obtain

$$\tan(2\theta) = \frac{B_x \tilde{r}_y + B_y \tilde{r}_x}{B_x \tilde{r}_x - B_y \tilde{r}_y} \quad (\text{A-12})$$

for the target azimuth producing the minimum response in a horizontal loop. In the limiting case of a point measurement of the dipolar secondary field, an identical expression is obtained, with $\tilde{\mathbf{r}}$ replaced by the vector between the source and measurement location. Taking a second derivative of equation A-11 yields the following condition satisfied at a minimum:

$$(B_x \tilde{r}_x - B_y \tilde{r}_y) \cos(2\theta_{\min}) + (B_y \tilde{r}_x + B_x \tilde{r}_y) \sin(2\theta_{\min}) < 0. \quad (\text{A-13})$$

Testing this condition at θ_{\min} and $\theta_{\min} + \pi/2$ identifies the azimuths producing a minimum and maximum of the vertical magnetic field in a given receiver. By inspection, we find that the vertical field can then be expressed as

$$B_z(\mathbf{r}, t) = a \sin(2\phi - \nu) + b. \quad (\text{A-14})$$

The amplitude a , phase ν , and DC offset b can all be inferred by predicting the data at the extrema determined using equation A-12. Figure A-1 shows agreement between equation A-14 and the data predicted by explicitly forming the polarizability tensor for each azimuth. Calculation with equation A-14 is approximately 2.5 times faster than the brute-force approach.

REFERENCES

- Bell, T., B. Barrow, and J. T. Miller, 2001, Subsurface discrimination using electromagnetic induction sensors: IEEE Transactions on Geoscience and Remote Sensing, **39**, 1286–1293, doi: [10.1109/36.927451](https://doi.org/10.1109/36.927451).
- Beran, L., B. Zelt, L. Pasion, S. Billings, K. Kingdon, N. Lhomme, L.-P. Song, and D. Oldenburg, 2012, Practical strategies for classification of unexploded ordnance: Geophysics, **78**, no. 1, E41–E46, doi: [10.1190/geo2012-0236.1](https://doi.org/10.1190/geo2012-0236.1).
- Bijamov, A., J. P. Fernández, B. E. Barrowes, I. Shamatava, K. O'Neill, and F. Shubitidze, 2014, Camp Butner live-site UXO classification using hierarchical clustering and Gaussian mixture modeling: IEEE Transactions on Geoscience and Remote Sensing, **52**, 5218–5229, doi: [10.1109/TGRS.2013.2287510](https://doi.org/10.1109/TGRS.2013.2287510).
- Billings, S. D., and K. A. Kingdon, 2008, UXO characterization: Comparing cued surveying to standard detection and discrimination approaches; ground penetrating radar for unexploded ordnance characterization: Technical report, United States Army Corps of Engineers, Engineering Research and Development Center.
- Butler, D. K., 2003, Implications of magnetic backgrounds for unexploded ordnance detection: Journal of Applied Geophysics, **54**, 111–125, doi: [10.1016/j.jappgeo.2003.08.022](https://doi.org/10.1016/j.jappgeo.2003.08.022).
- Delaney, W. P., and D. Etter, 2003, Report of the defense science board on unexploded ordnance: Technical report, Office of the Undersecretary of Defense for Acquisition, Technology and Logistics.
- Everett, M. E., 2013, Near-surface applied geophysics: Cambridge University Press.
- Fernandez, J. P., B. Barrowes, A. Bijamov, K. O'Neill, I. Shamatava, D. A. Steinhurst, and F. Shubitidze, 2012, Optimizing EMI transmitter and receiver configurations to enhance detection and identification of small and deep metallic targets: Proceedings of SPIE, 8357, Detection and Sensing of Mines, Explosive Objects, and Obscured Targets XVII, 835703, doi: [10.1117/12.919588](https://doi.org/10.1117/12.919588).
- Nelson, H. H., K. Kaye, and A. Andrews, 2010, Geophysical system verification (GSV): A physics-based alternative to geophysical prove-outs for munitions response: Technical report, ESTCP.
- Pasion, L. R., and D. W. Oldenburg, 2001, A discrimination algorithm for UXO using time domain electromagnetic induction: Journal of Environmental and Engineering Geophysics, **6**, 91–102, doi: [10.4133/JEEG6.2.91](https://doi.org/10.4133/JEEG6.2.91).
- Pasion, L. R., D. W. Oldenburg, S. D. Billings, and D. Sinex, 2007, Soil compensation techniques for the detection of buried metallic objects using electromagnetic sensors: Defense and Security Symposium, International Society for Optics and Photonics, 655326.
- Shamatava, I., F. Shubitidze, R. Joabava, B. E. Barrowes, K. O'Neill, and A. Bijamov, 2012, Application of the ONVMS model to discriminate challenging UXO targets: XVII International Seminar/Workshop on Direct and Inverse Problems of Electromagnetic and Acoustic Wave Theory (DIPED), 141–144.
- Smith, J. T., and H. F. Morrison, 2005, Optimizing receiver configurations for resolution of equivalent dipole polarizabilities in situ: IEEE Transactions on Geoscience and Remote Sensing, **43**, 1590–1498.